A Cyano-based Octanuclear $\{Fe^{III}_4Ni^{II}_4\}$ Single-Molecule Magnet

Yuanzhu Zhang,[a] Uma Prasad Mallik,[a] Nigam Rath,[a] Gordon T. Yee,[b] Rodolphe Clérac*,[cd] and Stephen M. Holmes*,[a]

[a] Department of Chemistry & Biochemistry, University of Missouri-St. Louis, St. Louis, MO 63121 (USA)

[b] Department of Chemistry, Virginia Polytechnic and State University, Blacksburg, VA 24061 (USA)

[c] CNRS, UPR 8641, Centre de Recherche Paul Pascal (CRPP), Equipe "Matériaux Moléculaires Magnétiques", 115 avenue du Dr. Albert Schweitzer, Pessac, F-33600, France

[d] Université de Bordeaux, UPR 8641, Pessac, F-33600, France

Synthesis of $[NEt_4]_2[(Tp^{*Me})Fe^{II}(CN)_3]\cdot H_2O$ (1). Drop wise addition of a 1:1 DMF/MeCN (40 mL) solution of $K(Tp^{*Me})$ (2.40 g, 6.36 mmol) in a DMF solution (20 mL) of $Fe(OAc)_2$ (2.20 g, 12.6 mmol) over 30 min. afforded a gray mixture that was evacuated to dryness after 3 h at 50° C. The remaining gray solid was extracted with MeCN (2 × 20 mL), filtered, and was added drop wise to a MeCN (30 mL) solution of $[NEt_4]CN$ (2.98 g, 19.1 mmol). The brown suspension was stirred for 4 h and filtered to remove a brown precipitate. The filtrate was concentrated to ca. 20 mL and addition of Et_2O (90 mL) afforded a red precipitate. The solid was isolated via suction filtration, washed with Et_2O (2 ×5 mL), and dried under vacuum for 2 min. Yield: 3.05 g (63.8%). Crystals are obtained from slow diffusion of Et_2O into a MeCN solution of $[NEt_4]_2[(Tp^{*Me})Fe^{II}(CN)_3]\cdot H_2O$. IR (Nujol, cm^{-1}): 2507 ($\tilde{\nu}_{BH}$, s), 2044 ($\tilde{\nu}_{CN}$, s).

Table S1. Crystallographic Data for $[NEt_4][(Tp^{*Me})Fe^{III}(CN)_3]\cdot H_2O$ (**1**) and $\{[(Tp^{*Me})Fe^{III}(CN)_3]_4$-$[Ni^{II}(tren)]_4[ClO_4]_4\}\cdot 7H_2O\cdot 4MeCN$ (**2**).

	1	**2**
crystal color	red	red
formula	$C_{29}H_{50}BFeN_{10}O$	$C_{58}H_{105}B_2Cl_2Fe_2N_{28}Ni_2O_{11.5}$
crystal system	monoclinic	triclinic
formula wt	621.45	1700.34
space group	$P2_1/n$	P-1
wavelength, Å	0.71073	0.71073
Temperature, K	100(2)	100(2)
a, Å	9.9051(6)	14.058(1)
b, Å	16.122(1)	14.568(1)
c, Å	20.399(1)	23.412(2)
α, deg	90	75.052(3)
β, deg	93.661(2)	77.373(3)
γ, deg	90	62.117(3)
V, $Å^3$	3250.8(4)	4067.5(5)
D_c, g cm^{-3}	1.270	1.338
Z	4	2
μ, mm^{-1}	0.503	0.941
R_1^a	0.0447	0.0622
wR_2^a	0.1414	0.1598

[a] $I \geq 2\sigma(I)$: $R_1 = \sum||F_o| - |F_c||/\sum|F_o|$, $wR_2=\{\sum[w(F_o^2-F_c^2)^2]/ \sum[w(F_o^2)^2]\}^{1/2}$

Table S2. Selected Bond Distances (Å) and Angles (°) for $[NEt_4][(Tp^{*Me})Fe^{III}(CN)_3]\cdot H_2O$ (**1**) and $\{[(Tp^{*Me})Fe^{III}(CN)_3]_4[Ni^{II}(tren)]_4[ClO_4]_4\}\cdot 7H_2O\cdot 4MeCN$ (**2**).

		1					**2**	
Fe1-C19	1.920(2)	C19-Fe1-C20	89.34(7)		Fe1-C1	1.921(4)	C1-Fe1-C2	86.2(2)
Fe2-C20	1.921(2)	C19-Fe1-C21	86.90(7)		Fe2-C2	1.919(4)	C1-Fe1-C3	90.8(2)
Fe1-C21	1.923(2)	C20-Fe1-C21	87.45(7)		Fe1-C3	1.935(4)	C2-Fe1-C3	89.2(2)
Fe1-N1	2.002(1)	C19-Fe1-N1	90.37(6)		Fe1-N8	2.001(4)	C1-Fe1-N8	92.2(2)
Fe1-N3	2.006(1)	C19-Fe1-N3	91.36(6)		Fe1-N10	1.979(4)	C1-Fe1-N10	92.5(2)
Fe1-N5	2.007(1)	C19-Fe1-N5	179.42(6)		Fe1-N12	2.021(4)	C1-Fe1-N12	177.3(2)
C19-N7	1.149(2)	N1-Fe1-N3	89.24(5)		Fe2-C4	1.921(5)	N8-Fe1-N10	98.9(2)
C20-N8	1.153(2)	N1-Fe1-N5	89.82(5)		Fe2-C5	1.932(5)	N8-Fe1-N12	90.0(1)
C21-N9	1.154(2)	N3-Fe1-N5	89.20(5)		Fe2-C6	1.927(6)	N10-Fe1-N12	89.0(2)
		Fe1-C19-N7	178.1(1)		Fe2-N14	2.009(4)	Fe1-C1-N1	179.3(5)
		Fe1-C20-N8	177.9(2)		Fe2-N16	1.997(4)	Fe1-C2-N2	179.4(4)
		Fe1-C21-N9	178.7(2)		Fe2-N18	1.981(4)	Fe1-C3-N3	172.3(4)
					Ni1-N2	2.038(4)	C4-Fe2-C5	84.3(2)
					Ni1-N3A	2.132(4)	C4-Fe2-C6	85.2(2)
					Ni1-N19	2.133(4)	C5-Fe2-C6	87.7(2)
					Ni1-N20	2.106(4)	C4-Fe2-N14	174.0(2)
					Ni1-N21	2.090(4)	C4-Fe2-N16	94.3(2)
					Ni1-N22	2.094(4)	C4-Fe2-N18	94.0(2)
					Ni2-N1	2.050(4)	N14-Fe2-N16	90.0(2)
					Ni2-N4	2.126(4)	N14-Fe2-N18	90.4(2)
					Ni2-N23	2.093(4)	N16-Fe2-N18	88.2(2)
					Ni2-N24	2.119(4)	Fe2-C4-N4	172.0(4)
					Ni2-N25	2.129(4)	Fe2-C5-N5	177.5(5)
					Ni2-N26	2.096(4)	Fe2-C6-N6	178.0(5)
					C1-N1	1.152(6)	N2-Ni1-N3	89.9(4)
					C2-N2	1.153(6)	N2-Ni1-N19	100.8(2)
					C3-N3	1.157(6)	N2-Ni1-N20	94.9(2)
					Fe1···Fe2	7.524(6)	N2-Ni1-N21	92.2(2)
					Ni1···Ni2	7.181(5)	N2-Ni1-N22	175.2(2)
							N3-Ni1-N19	84.0(2)
							N3-Ni1-N20	88.4(2)
							N3-Ni1-N21	176.5(2)
							N3-Ni1-N22	94.5(1)
							N19-Ni1-N20	162.5(2)
							N19-Ni1-N21	92.8(2)
							N19-Ni1-N22	81.6(2)
							Ni1-N2-C2	170.6(3)
							Ni1-N3-C3	158.7(4)
							N1-Ni2-N4	92.5(1)
							N1-Ni2-N23	90.2(2)
							N1-Ni2-N24	99.2(2)
							N1-Ni2-N25	95.8(1)
							N1-Ni2-N26	173.4(2)
							N4-Ni2-N23	176.7(2)
							N4-Ni2-N24	85.8(2)
							N4-Ni2-N25	84.9(2)
							N4-Ni2-N26	93.8(2)
							Ni2-N1-C1	175.1(4)
							Ni2-N4-C4	158.7(4)

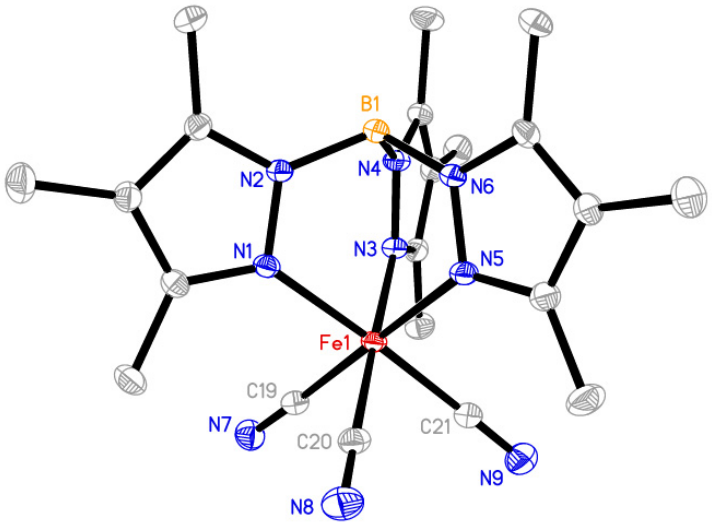

Figure S1. Truncated X-ray structure of **1**. All cations, lattice solvents, and hydrogen atoms are eliminated for clarity.

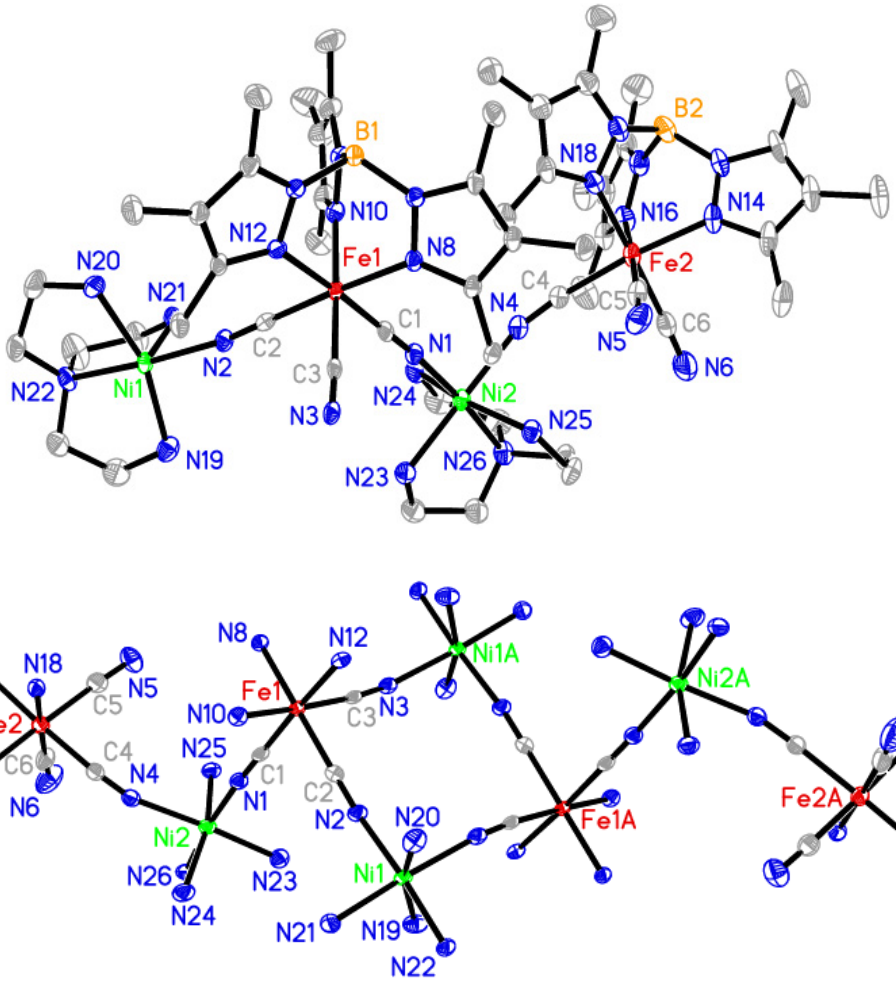

Figure S2. (top) Asymmetric unit of **2**. Note: Nearly parallel alignment of pseudo C_3 rotation axes. (bottom) Truncated structure of **2** showing octanuclear core of the complex.

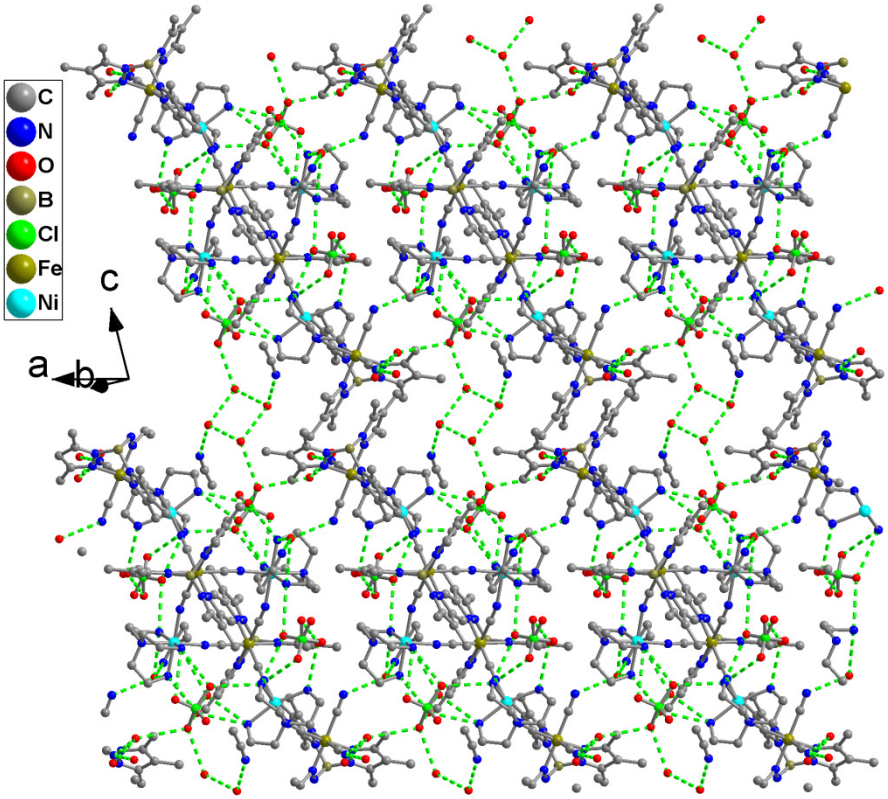

Figure S3. Packing diagram of **2** illustrating extensive hydrogen bonding interactions present within the *ab*-plane.

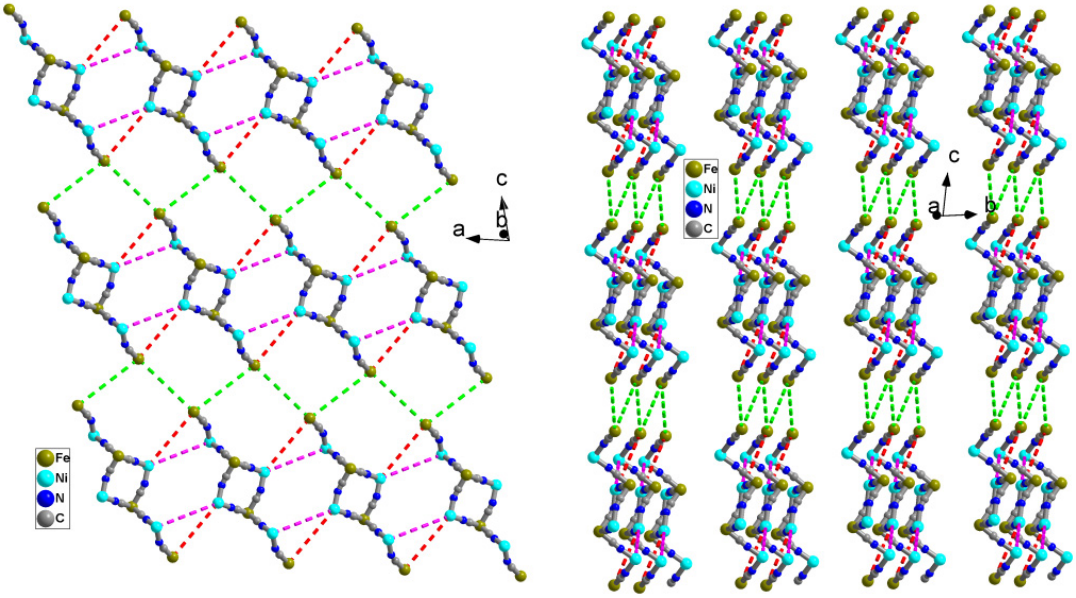

Figure S4. (left) Truncated packing arrangement of octanuclear cores present in complex **2** in the *ac*-plane. (right) Truncated packing arrangement of cores present in complex **2** in the *bc*-plane.

Magnetic properties of $[NEt_4][(Tp^{*Me})Fe^{III}(CN)_3]\cdot H_2O$ (1). At room temperature, the χT product for **1** is 0.66 cm^3.K/mol indicating an S = ½ spin ground state with a g factor around 2.65. Large g factors are expected for this type of $[L_3Fe^{III}(CN)_3]$ building blocks that display significant spin-orbit coupling effects. Indeed spin-orbit coupling is also responsible for the decrease of the χT product as the temperature is lowered (Figure S5 left). In the whole range of the temperature the Fe^{III} ion can be considered as an S = 1/2 spins as confirmed by the field dependence of the magnetization below 10 K that saturates at 1.8 K and 7 T around 1.1 μ_B.

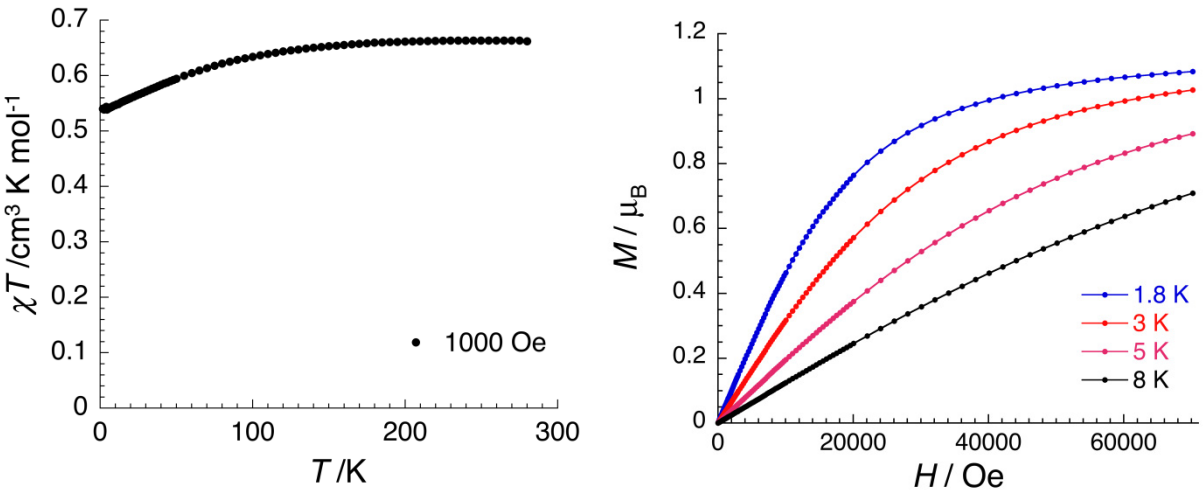

Figure S5. Left: χT vs T data for **1** (with χ defined as the magnetic susceptibility and equal to M/H) at 1000 Oe; Right: M vs H data for **1** below 8 K.

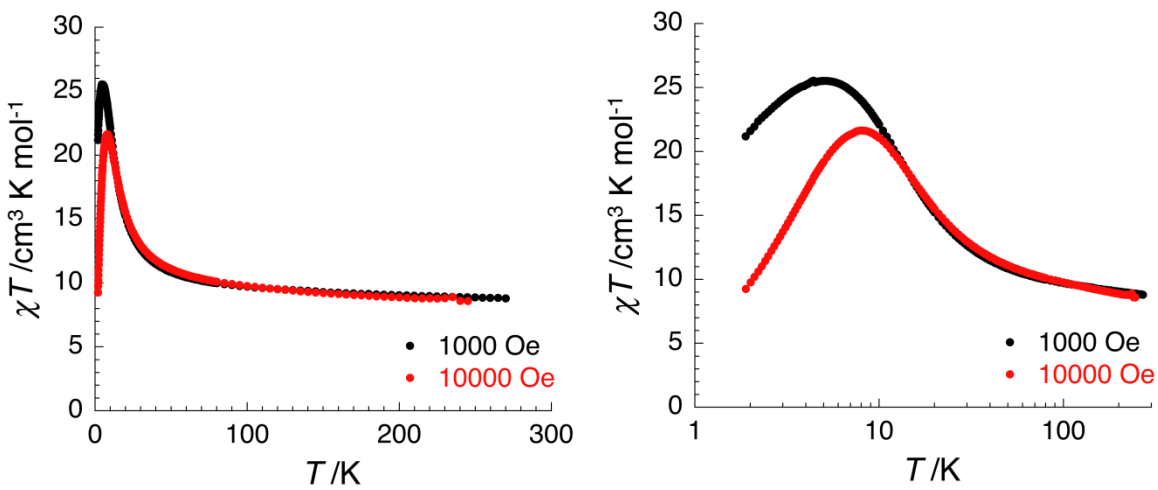

Figure S6. χT vs T data for **2** (with χ defined as the magnetic susceptibility and equal to M/H) at 1000 and 10000 Oe in linear (left) and semi-logarithmic plots (right), respectively.

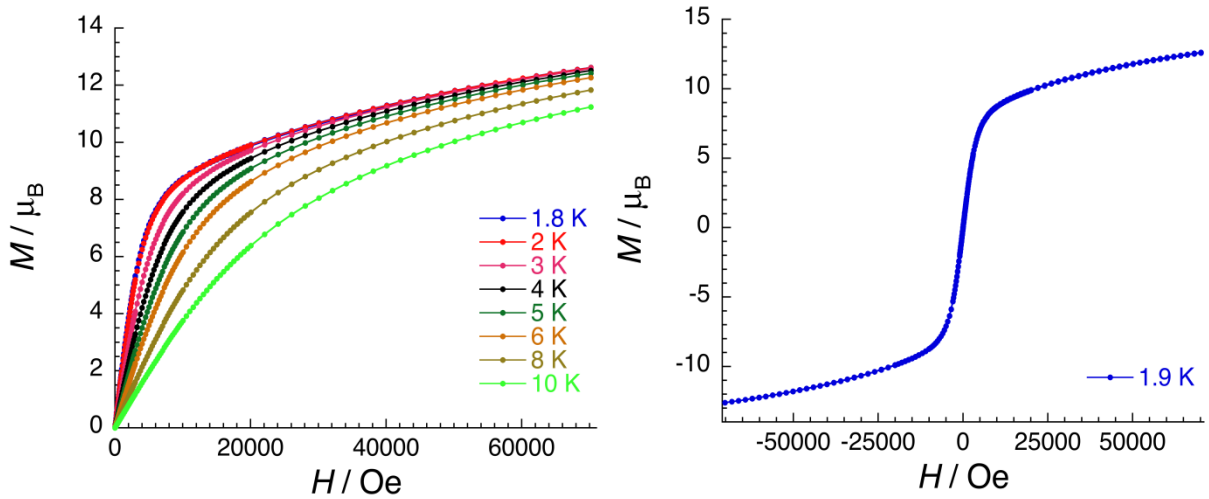

Figure S7. (left) *M* vs *H* data for **2** below 10 K. (right) *M* vs *H* data for **2** at 1.9 K.

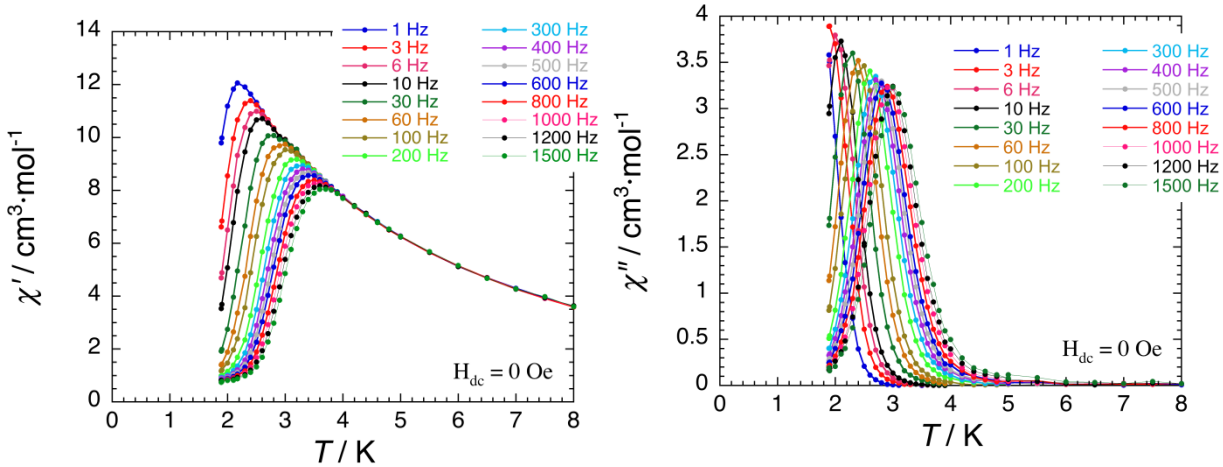

Figure S8. Temperature dependence of the in-phase (χ', left) and out-of-phase (χ'', right) components of the ac susceptibility between 1 and 1500 Hz (H_{ac} = 3 Oe; H_{dc} = 0 Oe) for **2** below 8 K. The solid lines are guides for the eyes.

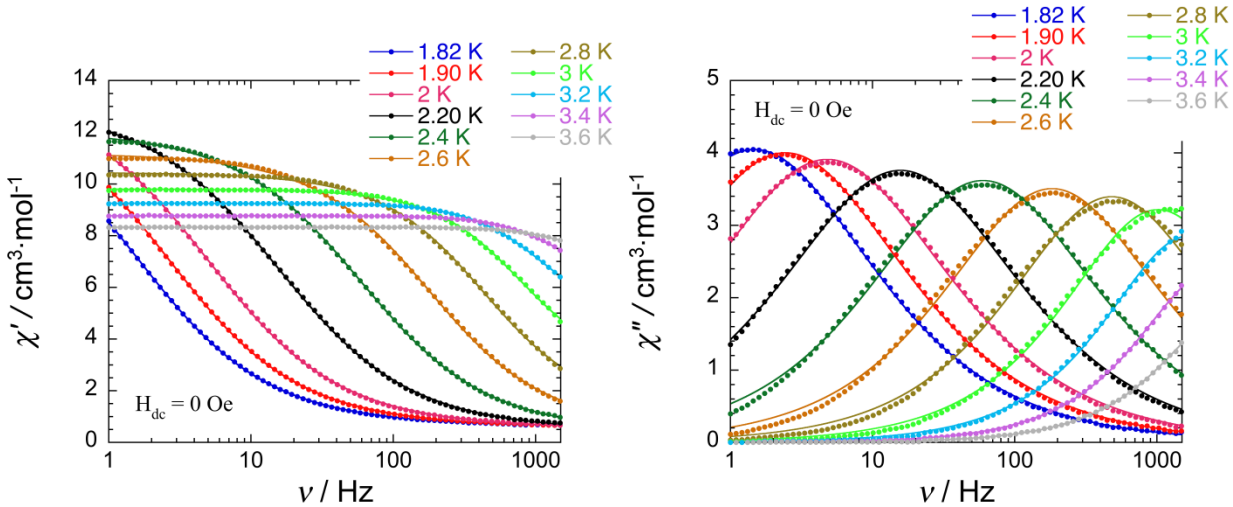

Figure S9. Frequency dependence of the in-phase (χ', left) and out-of-phase (χ'', right) components of the ac susceptibility at different temperatures between 1.8 and 3.6 K (H_{ac} = 3 Oe; H_{dc} = 0 Oe) for **2**. The solid lines are the best fits obtained with a generalized Debye model using α parameters consistently lower than 0.31.

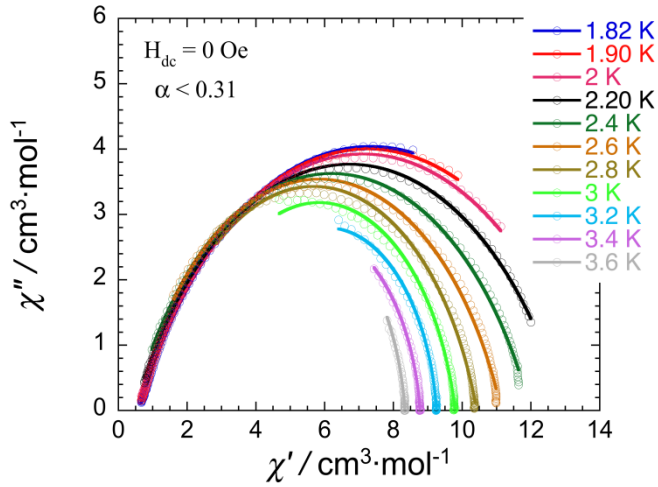

Figure S10. Cole-Cole plots at different temperature between 1.8 and 3.6 K for compound **2** measured in zero-dc field. The solid lines are the best fits obtained with a generalized Debye model using α parameters always lower than 0.31.

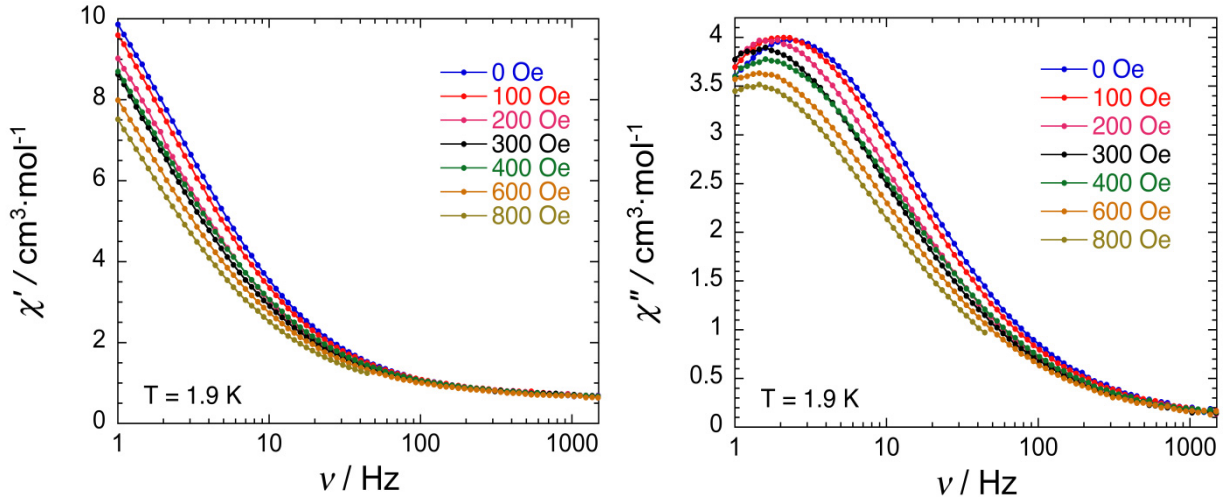

Figure S11. Frequency dependence of the in-phase (χ', left) and out-of-phase (χ'', right) components of the ac susceptibility at different applied dc fields ($0 \leq H_{dc} \leq 800$ Oe; $H_{ac} = 3$ Oe) for **2** at 1.9 K. The solid lines are guides for the eyes.